Lawrence Berkeley National Laboratory
Recent Work

Title

Revealing Anisotropic Spinel Formation on Pristine Li- and Mn-Rich Layered Oxide Surface and Its Impact on Cathode Performance

Authors

Kuppan, S
Shukla, AK
Membreno, D
et al.

ADVANCED
SCIENCE NEWS
www.advancedsciencenews.com

ADVANCED
ENERGY
MATERIALS
www.advenergymat.de

FULL PAPER

Revealing Anisotropic Spinel Formation on Pristine Li- and Mn-Rich Layered Oxide Surface and Its Impact on Cathode Performance

Saravanan Kuppan, Alpesh Khushalchand Shukla, Daniel Membreno, Dennis Nordlund, and Guoying Chen*

Surface properties of cathode particles play important roles in the transport of ions and electrons and they may ultimately dominate cathode's performance and stability in lithium-ion batteries. Through the use of carefully prepared $Li_{1.2}Ni_{0.13}Mn_{0.54}Co_{0.13}O_2$ crystal samples with six distinct morphologies, surface transition-metal redox activities and crystal structural transformation are investigated as a function of surface area and surface crystalline orientation. Complementary depth-profiled core-level spectroscopy, namely, X-ray absorption spectroscopy, electron energy loss spectroscopy, and atomic-resolution scanning transmission electron microscopy, are applied in the study, presenting a fine example of combining advanced diagnostic techniques with a well-defined model system of battery materials. The present study reports the following findings: (1) a thin layer of defective spinel with reduced transition metals, similar to what is reported on cycled conventional secondary particles in the literature, is found on pristine oxide surface even before cycling, and (2) surface crystal structure and chemical composition of both pristine and cycled particles are facet dependent. Oxide structural and cycling stabilities improve with maximum expression of surface facets stable against transition-metal reduction. The intricate relationships among morphology, surface reactivity and structural transformation, electrochemical performance, and stability of the cathode materials are revealed.

1. Introduction

Lithium- and manganese-rich layered transition metal oxides with a general formula of $Li_{1+x}M_{1-x}O_2$ (M = Ni, Mn, and Co, hereafter refer to as LMR-NMC) belong to a family of most promising cathode materials, capable of delivering capacities exceeding 250 mA h g^{-1} at a relatively high average operating potential of ≈3.6 V versus Li$^+$/Li.[1] In order to access such high capacity, the oxides must be activated in the first cycle.[2] This activation is characterized by an extended plateau between 4.5 and 4.6 V and associated with a large irreversible capacity loss.[3–5] Critical issues such as sluggish kinetics, voltage decay, dissolution of transition-metals (TMs), and high impedance at low state of charge (SOC) further prevent the commercial adaptation of these oxide cathodes.[6,7] Various studies have been carried out to understand the structural rearrangement occurring during cycling,[4,8,9] which is believed to be the root cause of the performance issues, but the results are often inconclusive or inconsistent and the proposed mitigating approaches so far have all met with limited success.[10–15]

LMR-NMCs have been traditionally described as "layered–layered composites" that consist of nanodomains of Li_2MnO_3 with a monoclinic C2/m structure and a layered LiMO$_2$ component with a trigonal R$\bar{3}m$ structure.[16] In recent years, studies using an array of advanced microscopies and spectroscopies have revealed the presence of a single-phase solid solution,[17–23] with entire bulk particles made up of a monoclinic C2/m structure clearly observed by Shukla et al.[23] It has been shown that the crystal structure of these complex oxides and their performance depend heavily on the composition and synthesis conditions. The common method of synthesizing LMR-NMC involves the coprecipitation of stoichiometric amounts of transition metal precursors, either hydroxides or carbonates, followed by sintering at 900–1000 °C in the presence of a lithium precursor, typically LiOH or Li_2CO_3.[24,25] This process is heterogeneous in nature and it often leads to the formation of micrometer-sized secondary agglomerates composed of primary particles with a variety of sizes and crystal facets. The nonuniformity is also manifested in elemental concentration gradient, particularly Li concentration, which is extremely sensitive to synthesis conditions due to its tendency to evaporate at high temperatures.[26] We believe this is one of the main reasons behind the different crystal structures observed by research groups. The unique structure complexity poses significant challenge in obtaining comprehensive understanding of the pristine materials, and most studies performed so far were based on LMR-NMC

Dr. S. Kuppan, Dr. A. K. Shukla,
Dr. D. Membreno, Dr. G. Chen
Energy Storage and Distributed Resources Division
Lawrence Berkeley National Laboratory
Berkeley, CA 94720, USA
E-mail: gchen@lbl.gov
Dr. D. Nordlund
Stanford Synchrotron Radiation Lightsource
SLAC National Accelerator Laboratory
Menlo Park, CA 94025, USA

ADVANCED
ENERGY
MATERIALS
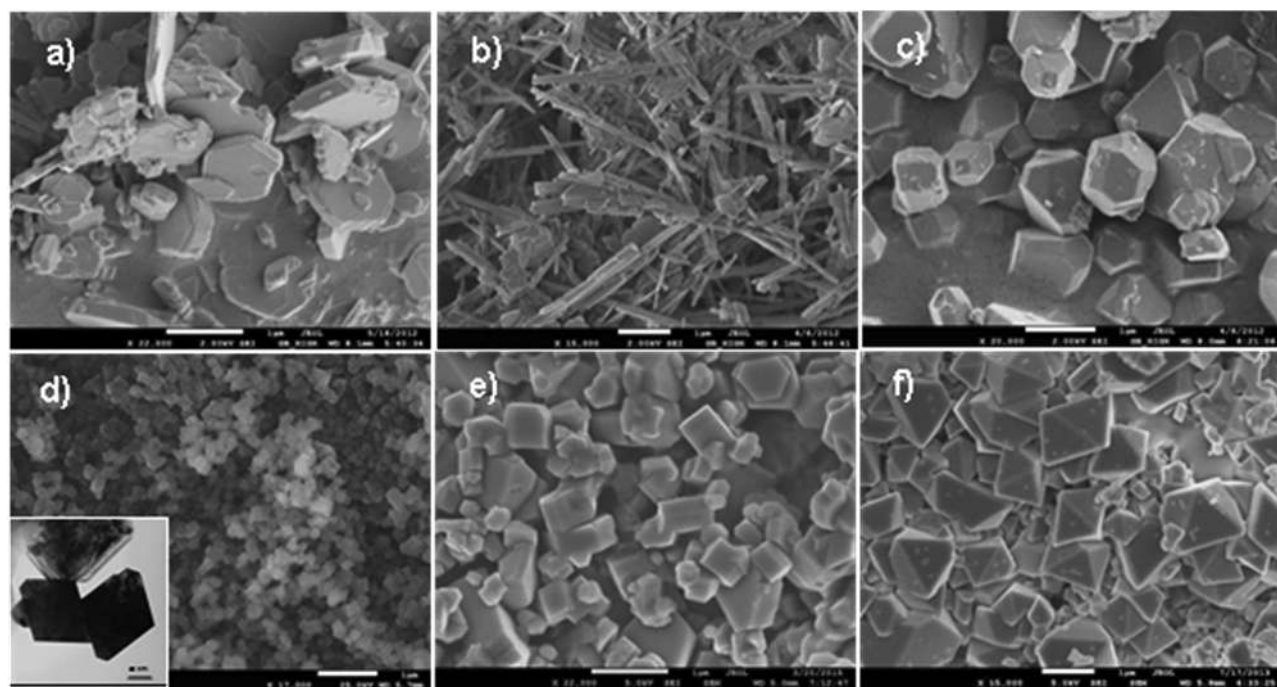www.advenergymat.de

ADVANCED
SCIENCE NEWS
www.advancedsciencenews.com

Figure 1. SEM images of $Li_{1.2}Ni_{0.13}Mn_{0.54}Co_{0.13}O_2$ crystal samples: a) plate, b) needle, c) L-Poly, d) S-Poly, e) box, and f) octahedron.

particles with poorly characterized bulk structure and pristine surface. On the other hand, quantification of cycling-induced bulk and surface changes is technologically significant as they hold the key to address the performance issues in these high-energy oxide cathodes.[6,7,23,27–29]

In a previous study, we investigated the bulk structure of $Li_{1.2}Ni_{0.13}Mn_{0.54}Co_{0.13}O_2$ (hereafter refer to as LMR-NMC141) and discovered a thin layer of spinel on some surface facets of the pristine needle-shaped crystals. This surface layer was found to be similar to what was previously reported as the "layered-to-spinel" surface transformation due to continuous cycling of LMR-NMC secondary particles. Recently, the use of LMR-NMC particles consisting of primary particles with preferred crystallographically oriented facets was also shown to minimize surface TM segregation and improve performance and stability.[30,31] To further understand the effect of surface facet on spinel formation and electrochemical performance of the cathode, we synthesized LMR-NMC141 crystal samples with six distinct morphologies by a molten-salt method.[32–34] The molten-salt technique utilizes a liquid reaction medium to enable atomic-level mixing of the reactants and allow for a homogeneous nucleation and growth of crystals from the flux at a relatively low temperature, which reduces Li loss during the synthesis and improves the uniformity and quality of the samples.[35] Here, we report the relationships among particle morphology, surface structural transformation, and electrochemical performance of LMR-NMCs. We highlight the importance of surface crystallographic plane in influencing cycling-induced surface changes and present particle engineering as a viable avenue in improving oxide performance. Material's design principles in addressing the critical issues facing this class of cathode materials are also discussed.

2. Results and Discussion

2.1. Synthesis and Properties of Pristine LMR-NMC141 Crystals

Molten-salt synthesis is commonly used to prepare transition-metal oxide crystals with high phase purity.[32,33,36] Several factors, including the chemical nature of the precursors and flux, the ratio between the TMs and the flux, reaction atmosphere, soaking temperature and time, and the heating and cooling rates, have been shown to be critical in influencing the uniformity and physical attributes of the synthesized samples.[37] **Figure 1** shows the scanning electron microscopy (SEM) images of six $Li_{1.2}Ni_{0.13}Mn_{0.54}Co_{0.13}O_2$ crystal samples synthesized in air in a covered alumina crucible. Plate-shaped crystals with an average size of 1 µm and a thickness of 200 nm (denoted as plate; Figure 1a) were obtained by reacting $LiNO_3$ and TM nitrate precursors in a CsCl flux (m. p. = 645 °C). The R ratio, which is defined as the molar ratio between the flux and the total transition metals, was controlled at 2. The mixture was maintained at 900 °C for 16 h before cooling to room temperature at a controlled rate of 3 °C min⁻¹. Needle-shaped crystals averaging 2 µm long and 50 nm in diameter (denoted as needle; Figure 1b) were obtained by using the same precursors in a KCl flux (m. p. = 770 °C), with an R ratio of 8 and a soaking condition of 800 °C for 8 h. Large polyhedron-shaped crystals in about 2 µm size (denoted as L-Poly; Figure 1c) were obtained when the TM oxides and Li_2CO_3 were used as precursors. The reaction was carried out in a CsCl flux with an R ratio of 8 and a soaking condition of 900 °C for 8 h. The mixture was then cooled to room temperature naturally. Small polyhedron-shaped crystals with an average size of about 200 nm (denoted as S-Poly; Figure 1d) were obtained after soaking the TM nitrates and Li_2CO_3 in a KCl flux at 850 °C for 8 h, with the

**ADVANCED
SCIENCE NEWS**

www.advancedsciencenews.com

**ADVANCED
ENERGY
MATERIALS**

www.advenergymat.de

FULL PAPER

Table 1. Synthesis conditions of the crystal samples.

Precursors	Li source	Flux	R	Temperature [°C]	Time [h]	Cooling rate [°C min⁻¹]	Samples
Nitrates	$LiNO_3$	CsCl	2	900	16	3	Plate
Nitrates	$LiNO_3$	KCl	8	800	8	3	Needle
Oxides	Li_2CO_3	CsCl	8	900	8	3	L-Poly
Nitrates	Li_2CO_3	KCl	8	850	8	3	S-Poly
Nitrates	$LiNO_3$	M_2CO_3 (M = Li, Na, K)	16	850	8	3	Box
Oxides	$LiNO_3$	M_2CO_3 (M = Li, Na, K)	8	850	8	3	Octahedron

R ratio controlled at 8. Micrometer-sized box-shaped (denoted as box; Figure 1e) and octahedron-shaped crystals (denoted as octahedron; Figure 1f) were prepared in a mixed alkali carbonate flux (M_2CO_3, M = Li, Na, and K) at 850 °C for 8 h, with TM nitrates and oxides as precursors. **Table 1** lists the detailed synthesis conditions for this series of LMR-NMC141 crystal samples.

The uniformity of all six samples was verified through extensive particle survey under SEM. The results showed that the crystal samples were highly uniform in morphology with more than 90% (estimation error: ±5%) of the crystals had the same shape as described for each sample. In each case, the crystals also had a narrow size distribution with more than 90% (estimation error: ±5%) particle size centered at the specified size region. The X-ray diffraction (XRD) patterns of the synthesized crystals are shown in Figure S1 (Supporting Information), where the expanded view in the region between 20° and 25° (2θ) is also shown in the inset. The peak features remain the same among the samples and they are similar to those reported in the literature,[38] confirming the phase purity and the lack of bulk structural difference among the samples. Further evaluation by high-angle annular dark-field (HAADF) scanning transmission electron microscopy (STEM) imaging confirms that the bulk of the particles in all samples adopted the same crystal structure as described in the previous publication.[23] In that study, microscopy and spectroscopy techniques at multilength scale were used to survey an entire LMR-NMC141 needle crystal, which revealed that contrary to the conventional notion of a composite structure consisting of trigonal and monoclinic phases, the bulk is made up of randomly stacked domains corresponding to three variants of the monoclinic structure (C2/m). Chemical compositions were verified by inductively coupled plasma (ICP) optical emission spectroscopic (OES) measurements, where the ratios between Li and transition metals were found to be

in good agreement with what was expected from the nominal composition of $Li_{1.2}Ni_{0.13}Mn_{0.54}Co_{0.13}O_2$. Alkali metals other than Li, namely, Na and K, were not found in the box or octahedron sample even though the synthesis procedure involved the use of a mixed alkali carbonate flux. Brunauer–Emmett–Teller (BET) surface area measurements showed that while the five micrometer-sized samples, plate, needle, L-Poly, box, and octahedron, had a similar surface area of about 0.3 m² g⁻¹, the smaller sized S-Poly sample had about ten times more surface area of about 3.0 m² g⁻¹. **Table 2** summarizes the sample composition determined by ICP as well as the surface area measured by BET.

Soft X-ray absorption spectroscopy (XAS) probes the transition-metal 3d electrons directly through dipole-allowed 2p to 3d transition, which can be used to investigate the average chemical properties of a large number of particles. Unlike the hard XAS technique, soft XAS (sXAS) is capable of differentiating the surface TM oxidation state from that of the bulk by using depth-resolved probing with three detection modes: Auger electron yield (AEY) that probes the top surface of 1–2 nm, total electron yield (TEY) that probes the depth of 2–5 nm, and fluorescence yield (FY) mode that collects signal from the bulk of the sample with a penetration depth of about 50 nm.[39] **Figure 2** shows Ni, Mn, and Co L-edge sXAS spectra of the pristine crystal samples in all three detection modes. The Ni spectra (Figure 2a) exhibit nearly identical line shapes and the same normalized intensities for L3 (Ni3p$_{3/2}$ fine structure, 851–857 eV) and L2 (Ni3p$_{1/2}$ fine structure, 869–874 eV) at all probing depths, suggesting that Ni remains at 2+ from the bulk to the surface in all samples. The Mn L-edge spectra consist of two well-defined absorption features in the L3 (639–647 eV) and L2 (650–657 eV) regions that are originated from the 2p core–hole spin-orbital splitting.[40] In general, Mn L-edge absorption features are dominated by the oxidation state and the

Table 2. Chemical composition and surface area of the crystal samples.

Samples	Experimental chemical composition [mol]				BET surface area [m² g⁻¹]
	Li	Mn	Ni	Co	
Plate	1.21 ± 0.04	0.53 ± 0.03	0.13 ± 0.01	0.13 ± 0.01	0.38
Needle	1.22 ± 0.05	0.53 ± 0.03	0.13 ± 0.01	0.13 ± 0.01	0.36
L-Poly	1.17 ± 0.03	0.57 ± 0.03	0.12 ± 0.01	0.12 ± 0.01	0.30
S-Poly	1.19 ± 0.02	0.54 ± 0.02	0.13 ± 0.01	0.13 ± 0.01	3.2
Box	1.22 ± 0.04	0.52 ± 0.03	0.14 ± 0.01	0.13 ± 0.01	0.30
Octahedron	1.12 ± 0.03	0.53 ± 0.02	0.12 ± 0.01	0.13 ± 0.01	0.31

ADVANCED
ENERGY
MATERIALS
www.advenergymat.de

ADVANCED
SCIENCE NEWS
www.advancedsciencenews.com

FULL PAPER
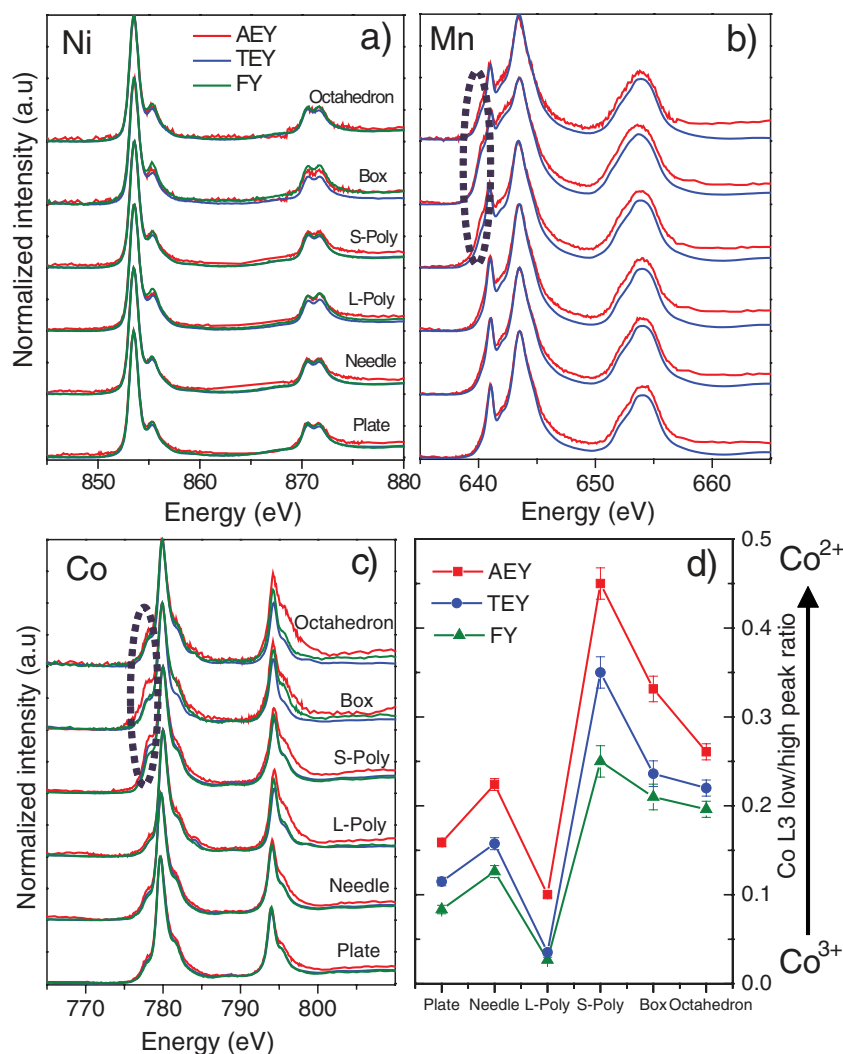
Figure 2. a–c) Soft XAS spectra of Mn, Co, and Ni *L*-edges collected on pristine Li$_{1.2}$Ni$_{0.13}$Mn$_{0.54}$Co$_{0.13}$O$_2$ crystal samples in AEY, TEY, and FY modes. The dashed ovals indicate the lower energy shoulder in Mn and Co *L*3-edges, and d) Co *L*3 low/high energy peak ratio of the crystal samples.

coordination of the cation.[41] Regardless of the crystal structure and ligands in the compound, manganese complexes with the same oxidation state in the octahedral sites always display similar *L*-edge absorption features, including the line shape and chemical shift. As a rule of thumb, the chemical shift moves downward for ≈2 eV in photon energy for each electron reduction in oxidation state.[42] As shown in Figure 2b, the Mn *L*3 edge spectra of the surface (AEY) and sub-surface (TEY) in the plate, needle, and L-Poly samples appear nearly identical and they are consistent with a Mn oxidation state of 4+ as reported in the literature.[41] On the other hand, the surface AEY spectra of the S-Poly, box, and octahedron samples show the presence of a lower-energy shoulder at ≈640 eV (highlighted with an oval in Figure 2b), which corresponds to a Mn oxidation state below 4+, although it is unclear whether Mn is at 2+ or 3+ state. This lower energy feature is also seen below the surface in the TEY *L*3 spectrum, suggesting more extensive reduction occurred in these samples. Similar to the Mn case, the fine structure

of Co *L*3 absorption edge (776–784 eV) provides the most salient knowledge on the electronic structure of cobalt, particularly the oxidation state.[43] As shown in Figure 2c, all three *L*3 spectra (AEY, TEY, and FY) of the plate, needle, and L-Poly samples are consistent with a Co oxidation state of 3+ as expected.[44] The surface AEY spectra of the S-Poly, box, and octahedron samples show significant enhancement in the low-energy peak cantered near 778 eV. Figure 2d summarizes the Co *L*3 peak ratio in the six pristine samples. An increase in the low/high energy peak ratio in Co *L*3 edge region indicates a decrease in unoccupied high-energy Co 3d state, which corresponds to Co reduction from 3+ to 2+.[39] The use of surface sensitive sXAS technique therefore allowed us to clearly detect the chemical gradient from the surface to bulk in some of the pristine LMR-NMC141 crystal samples. Except Ni, the surface TMs are at a lower oxidation state than that in the bulk. Particle morphology, more specifically crystal facet and surface area, appears to largely influence the extent of surface reduction during synthesis. The highest level of reduction observed on the S-Poly sample is likely due to its high surface area. The micrometer-sized box and octahedron samples closely followed the S-Poly sample and the least reduction was observed on the plate, needle, and L-Poly samples. The enhanced stability in the latter three samples suggests lower reactivity of the surface facets.

As sXAS provides ensemble-averaged information on the crystals, we then resorted to spatially resolved techniques, specifically aberration-corrected scanning transmission electron microscopy, electron energy loss spectroscopy (EELS), X-ray energy-dispersive spectroscopy (XEDS), and selected area electron diffraction (SAED), to differentiate surface atomic arrangements of the transition metals, crystal structure, and chemical composition from that in the bulk. **Figure 3**a shows the HAADF STEM image collected on an S-Poly crystal while Figure 3b shows an SAED pattern that was recorded using an aperture covering the entire particle. The SAED pattern shows an additional set of reflections along with those from the three variants of monoclinic C2/*m* structure, both of which are shown in the simulated SAED pattern (Figure 3c). The reflections from the secondary phase can be assigned to a spinel structure. Dark field images recorded using the spinel reflection (highlighted in the red circle) show that this phase is exclusively on particle surface, highlighted by the bright contrast in Figure 3d. The extent of spinel formation is nonuniform throughout the surface, which further confirms the facet-dependent nature. Co and Ni enrichment on the spinel surface was also observed when the spinel slab was parallel to the electron beam using other zone axes, as shown in the HAADF image and the XEDS maps in
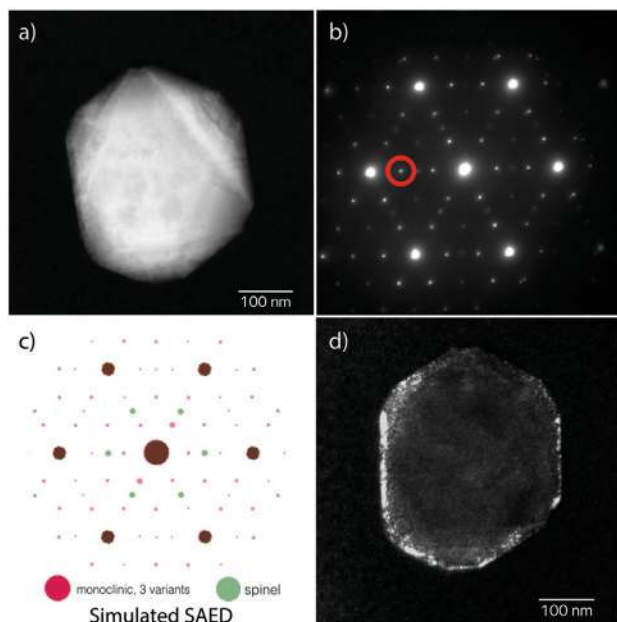
**ADVANCED
SCIENCE NEWS**
www.advancedsciencenews.com

**ADVANCED
ENERGY
MATERIALS**
www.advenergymat.de

Figure 3. a) HAADF STEM image collected on the S-Poly crystal sample, b) SAED pattern collected from the particle shown in (a), c) simulatd SAED pattern corresponding to the combination of C2/m and a spinel strucutre, and d) contrast image taken with the reflection shown in red in (b).

Figure S2 (Supporting Information). It should be noted that the facet consisting of spinel is not parallel to the direction of the electron beam in the HAADF image in Figure 3 and the transition metal enrichment is not seen in its XEDS maps in Figure S3 (Supporting Information).

Further evidence on pristine surface structural modification was provided by the STEM/EELS studies. **Figure 4**a,b shows the HAADF STEM images collected on a plate crystal in a low and a high-magnification, respectively. The large plate surfaces were identified as the $(001)_m$ plane, where m indicates a monoclinic lattice. A thin layer with a different atomic arrangement from that of the bulk is clearly seen on the surface, which has an estimated thickness of about 2 nm. Consistent with the previous survey on several particles in different orientations,[23] the crystal structure of the surface layer is a spinel where some lithium sites are occupied by the transition metals to form antisite defects. In the zone axis shown in Figure 4b, spinel oriented in [111] direction is observed on $(010)_m$ facets of the bulk monoclinic phase and on facets 120° from $(010)_m$, with an interface at $(33\bar{1})_m$. Surface spinel layer was not detected on the large surfaces of the plate or the $(001)_m$ facets, confirming that the layer to spinel phase transformation is directional. EELS data collected from the bulk to the surface that include the spectra of Mn, Ni, and Co L-edges are shown in Figure 4c and the $L3/L2$ ratio of each transition metal is shown in Figure 4d. Consistent with particle-assemble information obtained from sXAS, Ni remains at 2+ with its spectra showing no variation from the bulk to the surface. The spectra of both Mn and Co show a gradual increase in the $L3/L2$ ratio when going from the bulk toward the surface, corresponding to a decrease in oxidation state of both transition metals.[45,46] The results provide particle-level confirmation that Mn and Co are at lower

oxidation states on the surface and that the reduced TMs reside in a spinel-like instead of layered structure. All three transition metals are present in the surface spinel layer. The study also suggests that the transformation of layered-to-spinel in the Li- and Mn-rich layered oxides involves reduction of both Mn^{4+} and Co^{3+}, at least on the surface of the particle where the spinel structure is more defective.

A number of studies in the literature reported the presence of the surface spinel with reduced TMs on the cycled particles. The changes have been exclusively attributed to the effect of cycling while the surface of pristine particles was not fully defined.[8,9,47] We wish to bring it to the community's attention that the pristine samples, especially the secondary aggregates with a variety of crystal orientations commonly obtained from solid state synthesis, need to be carefully examined for structural and compositional inhomogeneity between the surface and the bulk. Furthermore, it is evident from this study that in order to determine the effect of battery cycling on structural transformations of the cathode surfaces, one has to ensure that the same crystalline orientation is examined for both pristine and cycled particles. These studies should also be performed in multiple zone axes to avoid the misinterpretations based on a particular 2D projection. The presence of a native surface layer with reduced TMs in a defective spinel structure is likely to alter the cathode–electrolyte interaction and influence structural transformation during the cycling of LMR-NMCs, both of which can have a significant impact on the performance and stability of this family of cathode materials. In the following sections, we investigate the electrochemical performance of the crystal samples and examine the various changes in the particles before and after cycling.

2.2. Electrochemical Performance of the LMR-NMC141 Crystals

$Li_{1.2}Ni_{0.13}Mn_{0.54}Co_{0.13}O_2$ crystal samples were prepared into composite electrodes, assembled into half cells, and then galvanostatically cycled between 2.5 and 4.6 V at a current density of 10 mA g^{-1}. **Figure 5**a shows the first-cycle charge and discharge voltage profiles where the typical features of the LMR-NMC cathodes are clearly shown. The charge profile consists of a slope region (where Li is extracted from the Li layer along with the oxidation of Ni^{2+} and possibly Co^{3+}) and an activation plateau region (where Li is extracted from the transition metal layer along with the TM diffusion and redox activities of oxygen). The corresponding charge capacity in each region and the discharge capacity are shown in Figure 5b. Except for the box sample that experienced a much higher polarization and lower overall capacity, the sloping region appears nearly identical in all samples and it accounts for a capacity of ≈100 mA h g^{-1}. Significant difference was observed on the plateau region, where the highest (255 mA h g^{-1}) and the lowest activation capacities (163 mA h g^{-1}) were found on the S-Poly and box samples, respectively, accounting for a difference of about 35%. It has been shown that the transport kinetics at the plateau region is nearly 1000 times slower than that in the slope region, owing to the need for a collective movement of the Li and TM cations, as well as oxygen in the lattice during the oxide activation.[48] This rate-limiting nature exacerbates
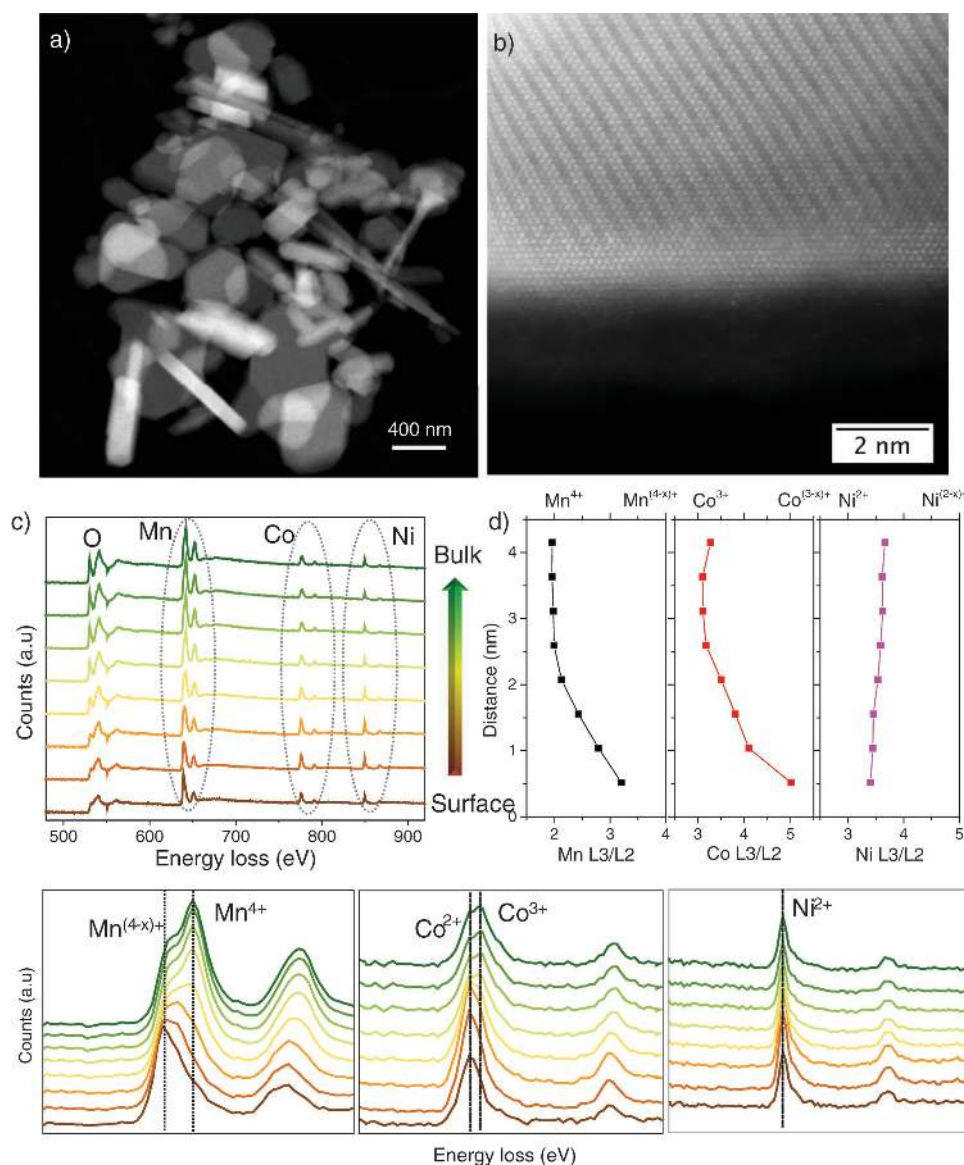
**ADVANCED
ENERGY
MATERIALS**

www.advenergymat.de

**ADVANCED
SCIENCE NEWS**

www.advancedsciencenews.com

Figure 4. a) Low and b) high-reolution HAADF STEM images collected on the plate sample, c) EELS spectra collected from the particle shown in the HAADF image in (b), with the expanded views shown at the bottom, and d) Ni, Co, and Mn *L3/L2* ratios determined from the EELS spectra in Figure 3c.

morphology effect in the region, as S-Poly with smaller particle size and higher surface area is kinetically more favorable and therefore more activated. Within the micrometer-sized particle series, the L-Poly and box samples had a relatively low plateau capacity of ≈165 mA h g^{-1} while all other samples had a similar plateau capacity of about 200 mA h g^{-1}, suggesting that morphology plays a role in kinetic properties as well. The total charge capacities of the samples were 303, 301, 264, 364, 258, and 293 mA h g^{-1} for plate, needle, L-Poly, S-Poly, box, and octahedron, respectively. The discharge capacity was found to be closely related to the length of the activation plateau, with S-Poly delivering the highest capacity of 277 mA h g^{-1}. The micrometer-sized plate, needle, and octahedron samples had a discharge capacity in the range of 205–235 mA h g^{-1} whereas much lower capacities were obtained on L-Poly (175 mA h g^{-1}) and the box samples (140 mA h g^{-1}). The results suggest that

both first cycle activation and discharge capacity are influenced by particle size and morphology. Within the series, the box morphology leads to inferior performance compared to the other morphologies. The comparison in rate capability of the samples is shown in Figure 5c. The trend in the kinetic behavior of the samples was found to be consistent with that in the activation and discharge capacities, with S-Poly and box being the best and worst performing samples, respectively.

Long-term cycling performance of the crystal samples was evaluated between 2.5 and 4.6 V at a current density of 20 mA g^{-1} and the capacity retention during the first 75 cycles is shown in Figure 5d. The samples can be divided into three groups: (1) plate, needle, and L-Poly with the least TM reduction on the pristine surface (as shown in Figure 2d) delivered the best cycling stability among the samples; (2) S-Poly and octahedron samples fall in the middle with a loss of about 30%
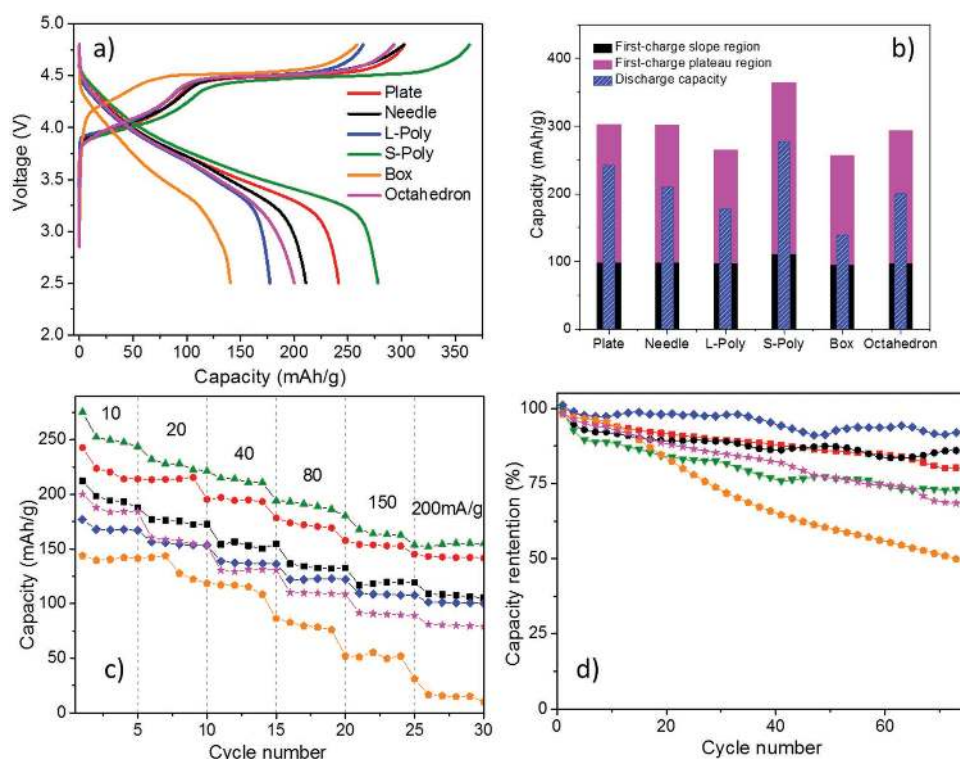
ADVANCED
SCIENCE NEWS
www.advancedsciencenews.com

ADVANCED
ENERGY
MATERIALS
www.advenergymat.de

Figure 5. a) First galvanostatic charge–discharge profiles of $Li_{1.2}Ni_{0.13}Mn_{0.54}Co_{0.13}O_2$ crystal samples at 10 mA g^{-1}, b) charge/discharge capacities of the first cycle, c) rate capability comparison of the crystal samples, and d) capacity retention of the half-cells cycled between 2.5 and 4.6 V at 20 mA g^{-1}.

capacity during the 75 cycles; and (3) the box sample had the worst performance, with a loss of nearly 50% capacity observed. Compared to the other micrometer-sized samples, the unusually high polarization of the voltage profile (Figure 5a), the much poorer kinetics and lower stability of the box sample suggest that it has more resistive surface facets that may also be more reactive toward side reactions.

Figure 6a shows the first 75 charge/discharge voltage profiles of the half cells with the various crystal cathodes. The experiments were performed following the current interrupt protocol described in the Experimental Section. In all cases, the charge/discharge endpoints gradually move toward the right (high capacity end) along with cycling, signaling the voltage slippage phenomenon that is often attributed to the parasitic reactions occurring between the cathode and the electrolyte in the lithium-ion battery (LIB) cells.[49,50] Monitoring this marching behavior of the capacity endpoint, therefore, has been used as a direct measure for the side reactivity contributing to battery failure. The voltage profiles in Figure 6a clearly show the impact of particle morphology and surface area, with significant more slippage observed on the S-Poly sample with a higher surface area and the box sample with the more reactive surface facets. Figure 6b summarizes the discharge capacity slippage as a function of cycle number in each sample. The trend in the marching rate is consistent with that in capacity retention shown in Figure 5d, with the least reactivity observed on the L-Poly and needle samples and the most on the box and S-poly samples, which also had the lowest and highest amount of TM reduction on the pristine surface, respectively.

Figure 7a shows the discharge voltage as a function of state of charge during the first 145 cycles collected on the plate sample. It is clear that below an SOC of about 80%, cell voltage gradually decreased along with cycling, a voltage fade phenomenon commonly observed in the LMR-NMC oxide cathodes. The behavior is considered as one of the most challenging barriers in commercializing this class of cathode materials as it gradually reduces the usable energy and efficiency of the battery cells. Although the exact mechanism remains unclear, which precludes the development of viable mitigation approaches, some studies suggested that structural rearrangement or an internal phase transition from the layered to spinel triggered by the migration of TM cations between the lithium and transition-metal layers is responsible for the voltage decay.[51] Voltage decay was observed on all our samples, suggesting that changes in crystal morphology and/or surface area do not completely stabilize the layered structure. However, the rate of decay was found to be sample dependent. Figure 7b compares the 25th cycle average discharge voltage as a function of the SOC of the samples. L-Poly outperformed all other samples at any given SOC whereas the box sample consistently discharged at lower voltage. This is consistent with the observed cycling stability and side reactivity, suggesting that bulk structural stability and voltage fade are also influenced by the surface properties and surface processes occurring during cycling. It is conceivable that the surface reactivity leads to the cation migration ultimately responsible for the detrimental structural rearrangement. Particularly, oxygen loss during the activation can create surface TM cations with the coordination of five oxygen anions, which is highly unstable. This may promote the
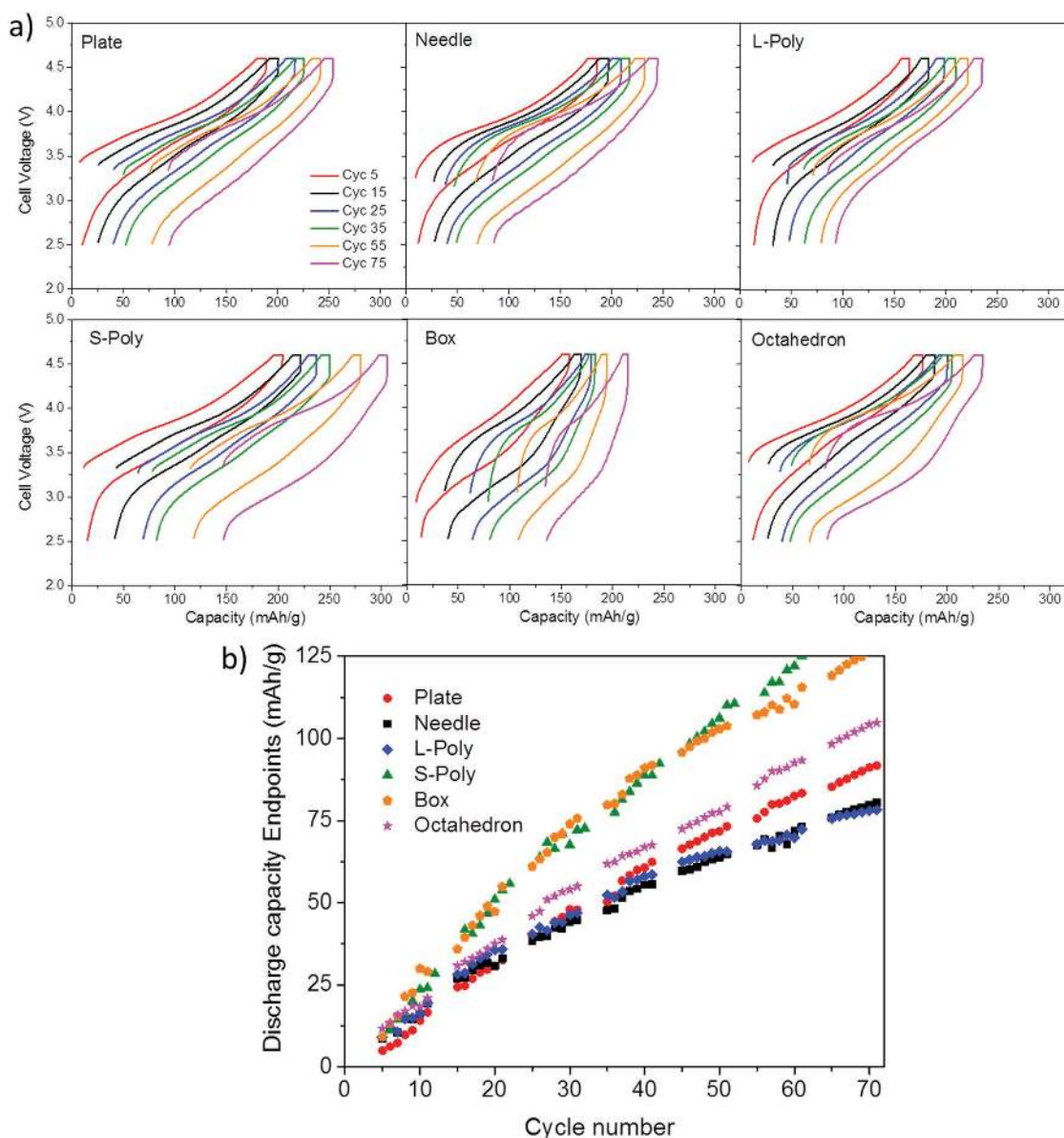
Figure 6. a) Voltage profiles of the samples during the first 75 cycles and b) discharge capacity slippage as a function of cycle number.

cations to migrate into the vacant octahedral sites left by the Li ions in the interslab, triggering the process of layered to spinel transformation. Although it remains unclear whether this is the most dominant process leading to bulk structural transformation in LMR-NMC oxides, the study highlights the importance of surface properties in influencing bulk changes. Particle engineering, therefore, presents an important avenue in addressing the challenging performance issues of the oxide cathodes and it should be further explored.

The average charge and discharge voltages were calculated by dividing the total cell energy (E) by the cell capacity (Q) at 4.6 V for charge and 2.5 V for discharge, respectively,[52] and their changes along cycling are shown in Figure 7c. The calculated average voltage values are expected to be slightly different from the true equilibrium values as polarization losses (iR) are not corrected here, but the data within the series are comparable.

Significant drop in charge voltage was observed between the first and second cycles due to the first-cycle activation. All samples showed a steady decrease in the discharge voltage along cycling. The slowest decay was found on the L-Poly sample and fastest on the box sample, consistent with the observation in Figure 7b. Figure 7d compares the voltage gaps between the charge and discharge at the 5th and 85th cycles. Except the box sample that had a much higher value of about 360 mV, all samples showed a similar gap of 260–300 mV at the fifth cycle. Upon continued cycling, the voltage gap between the charge and discharge increased as a result of gradual decay in average discharge voltage. At the 85th cycle, the gap increased to ≈500 mV for the plate, needle, and L-Poly samples while it increased to ≈750 mV in the box sample, a net change of nearly 400 mV. The results further corroborate with the trend observed in side reactivity and cycling stability.
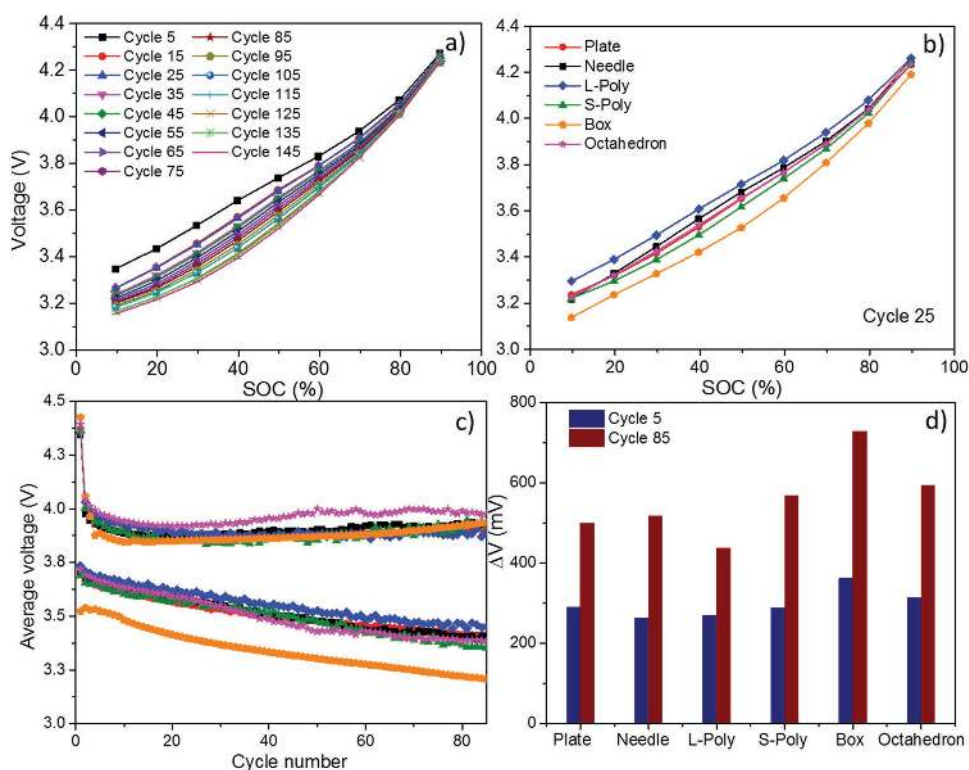
Figure 7. a) Average discharge voltage at various SOC of the plate sample as a function of cycle number, b) comparison of average discharge voltage as a function of SOC at cycle 25, c) average charge and discharge cell voltages as a function of cycle number, and d) comparison of charge–discharge voltage gaps at cycles 5 and 85.

2.3. Properties of Cycled LMR-NMC141 Crystals

For comparison, soft XAS measurements were performed on the cathodes recovered after 16, 30, and 45 cycles, respectively. In each case, the half-cell was fully discharged and carefully disassembled inside the glove box. The electrode was then thoroughly washed with dimethyl carbonate and dried under vacuum prior to the XAS measurement. As expected, Ni remains at 2+ in all samples and no significant changes were observed on the L-edge spectra after various cycling. Mn and Co L-edges, on the other hand, showed extensive changes in their spectral profiles, indicating modification in valence and coordination environment. **Figure 8**a shows the Mn $L2$ and $L3$ edge spectra of the surface (AEY) and the sub-surface (TEY) collected on the crystal electrodes. While Mn was shown in 4+ oxidation state in the pristine plate, needle, and L-Poly electrodes, a low-energy shoulder at the $L3$-peak (near 640 eV) after 16 cycles reveals the presence of lower valence manganese. Its intensity gradually increased with cycling, indicating continuous Mn reduction during electrochemical cycling. The intensity of the shoulder peak is also notably stronger in the AEY mode than that in the TEY mode, providing evidence that cycling-induced TM reduction progresses from the surface to the bulk. Similar behavior was also observed on S-Poly, box, and octahedron electrodes, which had reduced TMs on their pristine surface to begin with. Overall higher degree of TM reduction was observed on these samples, especially on the box sample where drastic changes in the $L3$ peak shapes of both AEY and TEY were observed after only 16 cycles. The results suggest that the

presence of reduced TM does not passivate the surface and further reduction continues during cycling.

The AEY, TEY, and FY Co $L3$ peak before (top) and after 45 cycles (bottom) are compared in Figure 8b. Cycling induces a gradual growth of the low-energy Co $L3$ shoulder peak at 778.2 eV, corresponding to the reduction of Co^{3+} to Co^{2+}, which was observed in all samples. Depth-dependent Co oxidation state gradient was also observed as the intensity of low-energy shoulder peak decreases in the order of AEY, TEY, and FY, confirming the progression of TM reduction from the surface to the bulk. Figure 8c shows the intensity ratio of Co $L3$ low/high energy peak in the cycled samples whereas the Figure 8d shows the net change in the ratio before and after cycling. Only FY data were used for net change comparison as saturation of Co^{2+} signal in AEY and/or TEY was observed on some cycled samples. Most extensive Co reduction was found on the box sample whereas the least was observed on the plate, needle, and L-Poly samples, the same trend observed in cycling stability (Figure 5d), side reactivity (Figure 6b), and cycling-induced voltage gap change (Figure 7d). Cycling promotes further TM reduction on the surface but at a different rate depending on the morphology and/or initial extent of TM reduction, demonstrating the important role of morphology in influencing surface reactivity of the oxide cathode particles. Moreover, the samples with the least cycling-induced reduction also had the lowest amount of TM reduction on the pristine surface, suggesting that the chemical composition of the pristine surface may be used as an indicator for surface reactivity of the sample. Detailed investigation on cycling-induced changes at the particle level is currently
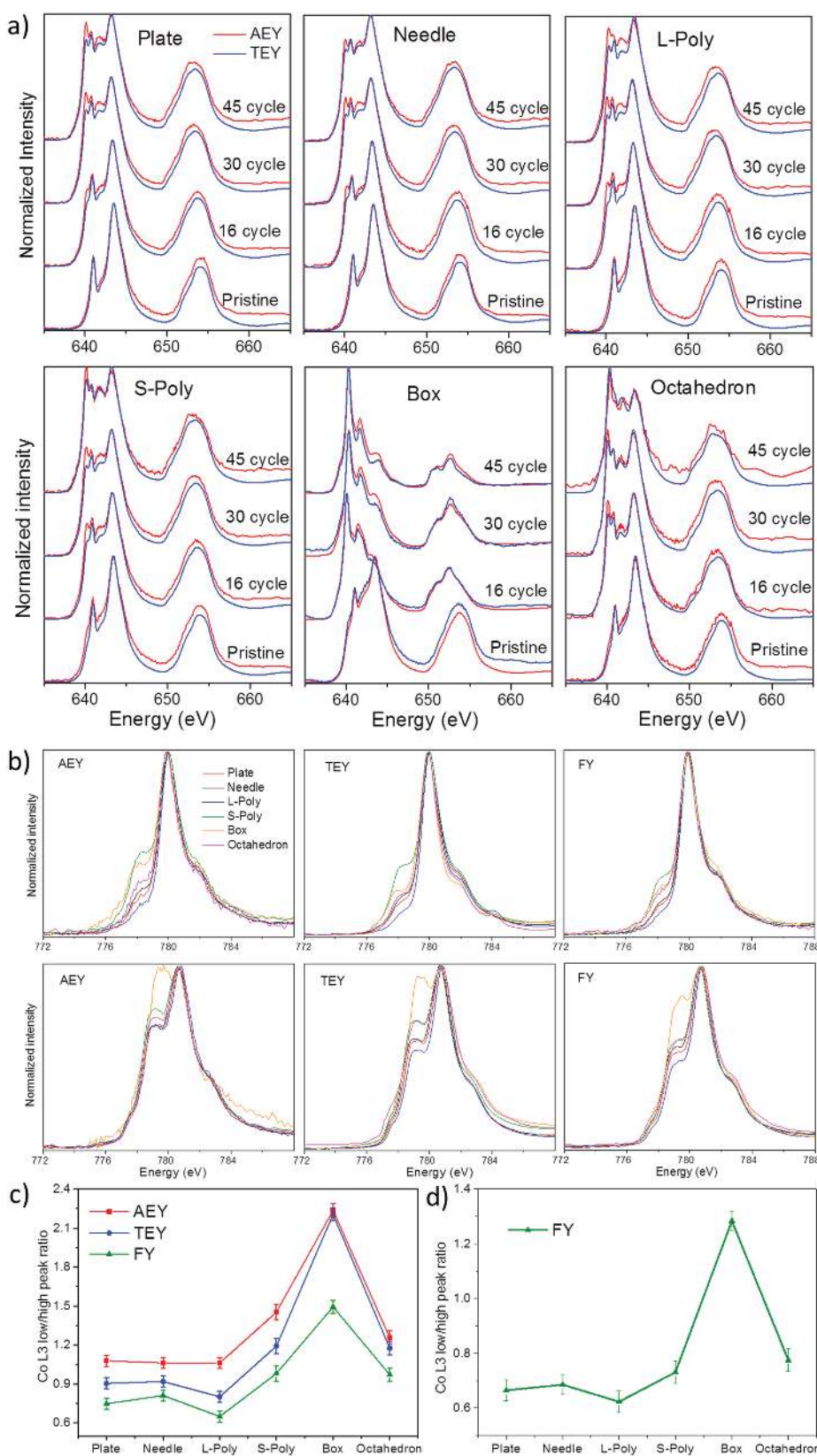
FULL PAPER

Figure 8. a) Mn *L*-edge sXAS spectra collected after the indicated number of cycles, b) Co *L*-edge sXAS spectra of the pristine electrodes (top) and electrodes recovered after 45 cycles (bottom), c) comparison of the Co low/high *L*3 peak ratio after cycling, and d) net changes in FY Co low/high *L*3 peak ratio before and after cycling.

underway and the results will be reported in a future publication.

Finally, we would like to point out that our attempts to completely characterize the crystal morphology of all samples by using projections at various zone axes in the electron microscope were met with severe difficulties. Determination of crystal facets based on this technique, combined with predictions based on the Wulff theorem, has been demonstrated for crystals with simple shapes.[53] In our case, however, it was challenging to characterize each facet of the samples due to the following factors: (1) the presence of varied amount of truncation in the polyhedrons within the same sample, (2) the presence of growth ledges that made the projection images more complicated, and (3) the microscope's limitation in titling at high angles. Crystal facet determination was also complicated due to the fact that these materials consist of several domains corresponding to three monoclinic variants, so a simple unit cell such as trigonal cannot be used for shape determination.

3. Conclusion

Six $Li_{1.2}Ni_{0.13}Mn_{0.54}Co_{0.13}O_2$ crystal samples with different sizes and crystal facets were synthesized by a molten-salt technique. A defective spinel layer with reduced transition metals was found on the surface of the pristine samples, more extensively on S-Poly, box, and octahedron than the plate, needle, and L-Poly samples. Careful analysis revealed that the formation of surface spinel phase is facet-dependent and it is largely absent in the direction where TM layer stacks. Cycling further promotes TM reduction that progresses from the surface toward the bulk, but the rate depends on particle morphology as well as the initial extent of TM reduction on the pristine. S-Poly, box, and octahedron samples with more extensive TM reduction on the pristine surface also had poorer capacity retention, higher side reactivity, and more excessive voltage fade. We correlated the

**ADVANCED
SCIENCE NEWS**

www.advancedsciencenews.com

**ADVANCED
ENERGY
MATERIALS**

www.advenergymat.de

FULL PAPER

difference observed in the electrochemical performance with particle morphology and surface spinel content on the pristine particles using an intricate electrochemical cycling protocol, high-resolution microscopy/spectroscopy, and high throughput ensemble-averaged spectroscopy, from which we reveal that particle morphology promoting clean surfaces without the presence of reduced transition metals is highly desirable for enhanced cathode performance and stability. We believe our findings will impact the general approach for tailoring the properties of LMR-NMCs as high-energy LIB cathodes.

4. Experimental Section

Crystal Synthesis: Unless otherwise specified, all chemicals were obtained from Aldrich with a purity of 97% or higher. Two synthesis routes were developed depending on the transition metal precursors used, namely, nitrates or oxides. For the nitrate route, stoichiometric amounts of $Mn(NO_3)_2$ $4H_2O$, $Co(NO_3)_2$ $6H_2O$, and $Ni(NO_3)_2$ $6H_2O$ were mixed with $LiNO_3$ or Li_2CO_3 in a chloride flux, either KCl or CsCl. The R ratio was controlled at either 2 or 8. The mixture was dissolved in a small amount of water that was removed by heating under agitation. The dried powder was transferred into an alumina crucible with a lid, heated to 800–900 °C at a rate of 3 °C min^{-1}, soaked at the high temperature for 8–16 h, and then cooled to room temperature at a controlled cooling rate. For the oxide route, stoichiometric amounts of MnO_2, Co_3O_4, NiO, and Li_2CO_3 were mixed with a CsCl flux ($R = 8$) in a shaker mill (8000M, SPEX SamplePrep) for 45 min. The mixture was then transferred into a covered alumina crucible, heated to 900 °C at a rate of 3 °C min^{-1}, soaked at 900 °C for 16 h, and then cooled naturally. In both cases, the final product was obtained by washing repeatedly with de-ionized water to remove the flux and then drying in a vacuum oven overnight at 80 °C.

Sample Characterization: XRD patterns were acquired using either a Bruker D2 Phaser or Panalytical X'Pert Pro diffractometer equipped with monochromatized Cu Kα radiation. The scans were collected from 10° to 80° (2θ) at a step size of 0.01° and a rate of 1.5 s per step. Lattice parameters and phase ratios were determined by full-pattern Rietveld refinements using Riqas (Materials Data, Inc.). Chemical composition analyses were performed on an ICP-OES (Perkin-Elmer Optima 5400). Surface area measurements were performed in an automatic gas adsorption analyzer (Micromeritics Tristar II 3020). Prior to the measurement, the samples were degassed for 4 h at 300 °C to remove surface water. A standard 5-point BET method based on N_2 adsorption at 77 K was used to determine the specific surface area. SEM images were collected on a JEOL JSM-7500F field emission microscope at a gentle beam mode with a 2 kV accelerating voltage. Samples for transmission electron microscopy (TEM) experiments were prepared by drop casting a sonicated solution of cathode particles in anhydrous ethanol onto a carbon-coated TEM grid. Selected area electron diffraction, dark-field imaging, and XEDS experiments were performed on an FEI Titan electron microscope operating at 120 kV accelerating voltage. HAADF images were collected using a probe-corrected scanning transmission electron microscope operating at a 100 kV accelerating voltage and a convergence angle of ≈30 mrad. The collection angle was calibrated at 82–190 mrad. EELS spectra were acquired using a Gatan Enfina spectrometer at low currents (below 40 pA) and the data were processed using principal component analysis, in order to improve the signal-to-noise ratio. For the soft X-ray absorption spectroscopy measurements, a thin layer of the cathode particles was spread onto a conductive carbon tape that was attached to an aluminum sample holder inside an Ar-filled glove box ($O_2 < 1$ ppm, $H_2O < 1$ ppm). Measurements were carried out on the 31-pole wiggler beamline 10–1 at Stanford Synchrotron Radiation Lightsource with a ring current of 350 mA, a 1000 L mm^{-1} spherical grating monochromator with 20 mm entrance and exit slits, a 0.2 eV energy resolution, and a 1 mm^2 beam spot. Data were collected at room

temperature under ultrahigh vacuum (10^{-9} Torr) in a single load using the AEY, TEY, and FY mode detectors.

Electrochemical Measurements: The composite electrodes were prepared by mixing 80 wt% of the LMR-NMC141 crystals with 5 wt% SFG-6 synthetic flake graphite (Timcal Ltd., Graphites and Technologies), 5 wt% acetylene carbon black (Denka), and 10 wt% Kynar 2801 poly(vinylidenefluoride) in an N-methyl methyl-pyrrolidone solution. The slurry was spread onto an aluminum foil and dried overnight at 80 °C under vacuum. The typical electrode loading is 4–5 mg cm^{-2}. Cathode disks with an area of 1.6 cm^2 were cut from the electrode sheets and assembled into 2032-type coin cells in an argon-filled glove box. Lithium foil (Alfa-Aesar) was used as counter and reference electrodes, Celgard 2400 polypropylene membrane as separators, and 1 M LiPF$_6$ in 1:1 ethylene carbonate:diethylene carbonate (Novolyte Technologies Inc.) was used as electrolyte. The cells were galvanostatically cycled between 2.5 and 4.8 V for the first-cycle and then 2.5 and 4.6 V for the rest of the cycles using a VMP3 multichannel potentiostat/galvanostat controlled by EC-Lab v10.12 software (BioLogic Science Instruments). The rate capability tests were performed by cycling the half cells at a current density of 10, 20 40, 80, 150, and 200 mA g^{-1}, each for five cycles. Current interrupt tests were carried out using the procedure established by Bettge et al.[52] The typical process involves C/5 charging to an upper cut-off voltage of 4.6 V and then holding at the voltage of 4.6 V for 30 min or until the current density decays to 1 µA cm^{-2}. Cells were discharged at a C/5 rate sequentially from 90% to 10% SOC with a step size of 10% SOC. SOC was determined by using the discharge capacity obtained from the previous C/5 cycle that was appropriately scaled to the discharge current of the cell. The analysis at each SOC was performed after 1 h rest at open circuit voltage (OCV) followed by a 1 C discharge pulse for 10 s. After an additional hour at OCV, the 1 C 10 s charge pulse was applied again. Cell voltage at each SOC was determined by tracking the voltage at the end of the OCV, prior to the discharge pulse. Average charge and discharge voltages were calculated by dividing the cell's total energy by the capacity measured at 4.6 V after charging and at 2.5 V after discharging, respectively.[52] Side reactivity was compared by tracking the charge/discharge endpoint marching shown as in the reports in the literature.[49,50] All electrochemical tests were carried out at room temperature.

Supporting Information

Supporting Information is available from the Wiley Online Library or from the author.

ADVANCED
ENERGY
MATERIALS

www.advenergymat.de

ADVANCED
SCIENCE NEWS

www.advancedsciencenews.com

FULL PAPER

[1] M. M. Thackeray, S.-H. Kang, C. S. Johnson, J. T. Vaughey, R. Benedek, S. Hackney, *J. Mater. Chem.* **2007**, *17*, 3112.

[2] A. R. Armstrong, M. Holzapfel, P. Novák, C. S. Johnson, S.-H. Kang, M. M. Thackeray, P. G. Bruce, *J. Am. Chem. Soc.* **2006**, *128*, 8694.

[3] N. Yabuuchi, K. Yoshii, S.-T. Myung, I. Nakai, S. Komaba, *J. Am. Chem. Soc.* **2011**, *133*, 4404.

[4] D. Mohanty, S. Kalnaus, R. A. Meisner, K. J. Rhodes, J. Li, E. A. Payzant, D. L. Wood, C. Daniel, *J. Power Sources* **2013**, *229*, 239.

[5] S. K. Martha, J. Nanda, G. M. Veith, N. J. Dudney, *J. Power Sources* **2012**, *199*, 220.

[6] J. R. Croy, M. Balasubramanian, K. G. Gallagher, A. K. Burrell, *Acc. Chem. Res.* **2015**, *48*, 2813.

[7] M. M. Thackeray, C. Wolverton, E. D. Isaacs, *Energy Environ. Sci.* **2012**, *5*, 7854.

[8] A. Boulineau, L. Simonin, J.-F. Colin, C. Bourbon, S. Patoux, *Nano Lett.* **2013**, *13*, 3857.

[9] M. Gu, I. Belharouak, J. Zheng, H. Wu, J. Xiao, A. Genc, K. Amine, S. Thevuthasan, D. R. Baer, J.-G. Zhang, *ACS Nano* **2012**, *7*, 760.

[10] S.-H. Kang, M. M. Thackeray, *Electrochem. Commun.* **2009**, *11*, 748.

[11] Y. K. Sun, M. J. Lee, C. S. Yoon, J. Hassoun, K. Amine, B. Scrosati, *Adv. Mater.* **2012**, *24*, 1192.

[12] Z. Li, Y. Zhang, H. Xiang, X. Ma, Q. Yuan, Q. Wang, C. Chen, *J. Power Sources* **2013**, *240*, 471.

[13] S. Shi, J. Tu, Y. Tang, X. Liu, Y. Zhang, X. Wang, C. Gu, *Electrochim. Acta* **2013**, *88*, 671.

[14] J.-S. Kim, C. S. Johnson, J. T. Vaughey, M. M. Thackeray, S. A. Hackney, W. Yoon, C. P. Grey, *Chem. Mater.* **2004**, *16*, 1996.

[15] J.-K. Noh, S. Kim, H. Kim, W. Choi, W. Chang, D. Byun, B.-W. Cho, K. Y. Chung, *Sci. Rep.* **2014**, *4*, 4847.

[16] C. Johnson, J. Kim, C. Lefief, N. Li, J. Vaughey, M. Thackeray, *Electrochem. Commun.* **2004**, *6*, 1085.

[17] K. A. Jarvis, Z. Deng, L. F. Allard, A. Manthiram, P. J. Ferreira, *Chem. Mater.* **2011**, *23*, 3614.

[18] H. Koga, L. Croguennec, P. Mannessiez, M. Ménétrier, F. o. Weill, L. Bourgeois, M. Duttine, E. Suard, C. Delmas, *J. Phys. Chem. C* **2012**, *116*, 13497.

[19] C. Genevois, H. Koga, L. Croguennec, M. Ménétrier, C. Delmas, F. Weill, *J. Phys. Chem. C* **2015**, *119*, 75.

[20] Z. Lu, Z. Chen, J. R. Dahn, *Chem. Mater.* **2003**, *15*, 3214.

[21] K. Jarvis, Z. Deng, A. Manthiram, P. J. Ferreira, L. Allard, *Microsc. Microanal.* **2012**, *18*, 1414.

[22] K. Jarvis, Z. Deng, A. Manthiram, P. Ferreira, *Microsc. Microanal.* **2012**, *18*, 1484.

[23] A. K. Shukla, Q. M. Ramasse, C. Ophus, H. Duncan, F. Hage, G. Chen, *Nat. Commun.* **2015**, *6*, 8711.

[24] X. Yang, X. Wang, G. Zou, L. Hu, H. Shu, S. Yang, L. Liu, H. Hu, H. Yuan, B. Hu, *J. Power Sources* **2013**, *232*, 338.

[25] H. Zhang, Q. Qiao, G. Li, S. Ye, X. Gao, *J. Mater. Chem.* **2012**, *22*, 13104.

[26] C.-C. Wang, K. A. Jarvis, P. J. Ferreira, A. Manthiram, *Chem. Mater.* **2013**, *25*, 3267.

[27] M. M. Thackeray, C. S. Johnson, J. T. Vaughey, N. Li, S. A. Hackney, *J. Mater. Chem.* **2005**, *15*, 2257.

[28] Z. Lu, J. R. Dahn, *J. Electrochem. Soc.* **2002**, *149*, A815.

[29] M. Sathiya, G. Rousse, K. Ramesha, C. Laisa, H. Vezin, M. T. Sougrati, M.-L. Doublet, D. Foix, D. Gonbeau, W. Walker, *Nat. Mater.* **2013**, *12*, 827.

[30] F. Yang, Y. Liu, S. K. Martha, Z. Wu, J. C. Andrews, G. E. Ice, P. Pianetta, J. Nanda, *Nano Lett.* **2014**, *14*, 4334.

[31] H. Dixit, W. Zhou, J.-C. Idrobo, J. Nanda, V. R. Cooper, *ACS Nano* **2014**, *8*, 12710.

[32] G. Chen, B. Hai, A. K. Shukla, H. Duncan, *J. Electrochem. Soc.* **2012**, *159*, A1543.

[33] B. Hai, A. K. Shukla, H. Duncan, G. Chen, *J. Mater. Chem. A* **2013**, *1*, 759.

[34] H. Duncan, B. Hai, M. Leskes, C. P. Grey, G. Chen, *Chem. Mater.* **2014**, *26*, 5374.

[35] T. Kimura, *Molten Salt Synthesis of Ceramic Powders*, INTECH Open Access Publisher, New York **2011**.

[36] S. Kuppan, H. Duncan, G. Chen, *Phys. Chem. Chem. Phys.* **2015**, *17*, 26471.

[37] P. Afanasiev, C. Geantet, *Coord. Chem. Rev.* **1998**, *178*, 1725.

[38] H. Koga, L. Croguennec, M. Ménétrier, K. Douhil, S. Belin, L. Bourgeois, E. Suard, F. Weill, C. Delmas, *J. Electrochem. Soc.* **2013**, *160*, A786.

[39] F. Lin, D. Nordlund, I. M. Markus, T.-C. Weng, H. L. Xin, M. M. Doeff, *Energy Environ. Sci.* **2014**, *7*, 3077.

[40] W. Yang, X. Liu, R. Qiao, P. Olalde-Velasco, J. D. Spear, L. Roseguo, J. X. Pepper, Y.-d. Chuang, J. D. Denlinger, Z. Hussain, *J. Electron. Spectrosc. Relat. Phenom.* **2013**, *190* (Part A), 64.

[41] W. Yang, X. Liu, R. Qiao, P. Olalde-Velasco, J. D. Spear, L. Roseguo, J. X. Pepper, J. D. Denlinger, Z. Hussain, *J. Electron. Spectrosc. Relat. Phenom.* **2013**, *190*, 64.

[42] M. Grush, J. Chen, T. Stemmler, S. George, C. Ralston, R. Stibrany, A. Gelasco, G. Christou, S. Gorun, J. Penner-Hahn, *J. Am. Chem. Soc.* **1996**, *118*, 65.

[43] A. M. Hibberd, H. Q. Doan, E. N. Glass, F. M. F. de Groot, C. L. Hill, T. Cuk, *J. Phys. Chem. C* **2015**, *119*, 4173.

[44] W.-S. Yoon, K.-B. Kim, M.-G. Kim, M.-K. Lee, H.-J. Shin, J.-M. Lee, J.-S. Lee, C.-H. Yo, *J. Phys. Chem. B* **2002**, *106*, 2526.

[45] H. K. Schmid, W. Mader, *Micron* **2006**, *37*, 426.

[46] Z. Wang, J. Bentley, N. Evans, *Micron* **2000**, *31*, 355.

[47] B. Xu, C. R. Fell, M. Chi, Y. S. Meng, *Energy Environ. Sci.* **2011**, *4*, 2223.

[48] A. van Bommel, J. Dahn, *Electrochem. Solid-State Lett.* **2010**, *13*, A62.

[49] A. Smith, J. Burns, D. Xiong, J. Dahn, *J. Electrochem. Soc.* **2011**, *158*, A1136.

[50] J. Xu, R. D. Deshpande, J. Pan, Y.-T. Cheng, V. S. Battaglia, *J. Electrochem. Soc.* **2015**, *162*, A2026.

[51] P. K. Nayak, J. Grinblat, M. Levi, B. Markovsky, D. Aurbach, *J. Electrochem. Soc.* **2014**, *161*, A1534.

[52] M. Bettge, Y. Li, K. Gallagher, Y. Zhu, Q. Wu, W. Lu, I. Bloom, D. P. Abraham, *J. Electrochem. Soc.* **2013**, *160*, A2046.

[53] T. Duden, A. Gautam, U. Dahmen, *Ultramicroscopy* **2011**, *111*, 1574.